

Investigation of Corroded T91 Steel in Static Lead-Bismuth Eutectic Under an Oxidising Environment

Minyi Zhang^{1*}, Weiyue Zhou³, Michael P. Short³, Paul A.J. Bagot¹, Michael P. Moody^{1,4},
and Felix Hofmann^{2*}

¹ Department of Materials, University of Oxford, Parks Road, Oxford, OX1 3PH, United Kingdom.

² Department of Engineering Science, University of Oxford, Parks Road, Oxford, OX1 3PJ, United Kingdom.

³Department of Nuclear Science and Engineering, Massachusetts Institute of Technology, 77 Massachusetts Avenue, Cambridge, MA 02139, USA.

⁴Australia's Nuclear Science and Technology Organisation, New Illawarra Road, Sydney, Lucas Heights NSW 2234, Australia.

* Corresponding authors:

Minyi Zhang (minyi.zhang@materials.ox.ac.uk, +44 7552534149),

Felix Hofmann (felix.hofmann@eng.ox.ac.uk, +44 1865283446)

Abstract

Understanding corrosion in liquid metal-cooled nuclear systems is tantamount to controlling it. While much literature exists detailing corrosion rates and mechanisms of structural materials in liquid metals, much still remains to be discovered in new regimes of temperature, chemistry, and impurity levels. We focus on a less-studied

set of conditions, specifically to investigate how liquid lead-bismuth eutectic (LBE) corrodes ferritic/martensitic steels in high-temperature oxidizing conditions. We find that corrosion follows grain boundaries, transitioning from intergranular attack to broader area corrosion as it progresses. Both the Cr and oxygen diffusion play vital roles in this process. Mechanistically speaking, the ingress of LBE induces regions of martensitic decomposition to ferrite via localized Cr depletion, somewhat blunting or slowing the corrosion from occurring. A stable, coherent oxide scale appears to be the deciding factor controlling whether intergranular LBE attack occurs or not. Most surprisingly, a layer of Fe enriched BCC phase forms on the surface of LBE-corroded T91 at these conditions, contradicting previous studies, including our own, which reported oxide-based surface layers.

1. Introduction

Liquid metals, such as lead–bismuth eutectic (LBE), pure lead (Pb), and lead–lithium (PbLi) alloys, are considered promising candidate coolants for Generation IV fast nuclear fission reactors, magnetic confinement fusion reactors, and concentrated solar power systems. These coolants possess several advantageous properties [1], including low neutron moderation and capture cross-sections, low melting points, low vapor pressures, wide margins to boiling, excellent gamma radiation shielding, and relatively low reactivity with water and air [2]. Interest in these systems has been further stimulated by the growing global emphasis on mitigating climate change and reducing CO₂ emissions [3].

T91, a ferritic–martensitic (F/M) steel, is a leading candidate structural material for these high-temperature energy systems. It exhibits excellent resistance to irradiation-

induced void swelling [4], along with low thermal expansion, relatively high thermal conductivity, widely tunable strength and creep resistance (critical for high-temperature operation), and a well-established supply chain with ASME nuclear qualification [5]. Compared with martensitic steels of higher chromium content, T91 demonstrates a smaller irradiation-induced ductile-to-brittle transition temperature (DBTT) shift. According to the research of Kohyama, at 250°C, with 0.8 dpa irradiation, DBTT shift for 9CrWVTa steels is around 24°C while for 11CrMoVNb steels the number will reach 175°C [6]. Moreover, F/M steels such as T91 mitigate the problem of accelerated corrosion at temperatures above 500 °C, in contrast to austenitic steels where fertilization of the austenite phase is promoted [7]. In this work, we focus on the use of T91 in conjunction with LBE for the design of LBE-cooled fast reactors (LBEFRs). Fast reactors are regarded as a key technology for enhancing the sustainability of nuclear energy, as they enable more efficient utilization of existing nuclear waste, allow for easier closing of the fuel cycle, and contribute to the reduction of the long-term radioactivity of spent fuel [8].

To further enhance the efficiency and economic viability of LBEFRs, this study investigates corrosion of T91 in LBE at elevated temperatures exceeding 700 °C, which would decisively boost electrical conversion efficiency and enable the usage of high-temperature process heat for other industrial purposes. Such high operating temperatures are achievable with LBE, unlike with water, and represent one of the key advantages motivating the adoption of this coolant. However, corrosion of structural steels becomes increasingly severe under these conditions, and thus remains a major bottleneck in the further development and deployment of LBEFRs.

Passivation is a commonly adopted strategy to enhance the corrosion resistance of structural materials by forming a stable and protective oxide layer on the steel surface, thereby minimizing direct contact between the liquid metal and the substrate [9]. For example, the Russian SVBR reactor design relies on the formation of an oxide layer to protect structural components [10]. According to literature, maintaining an oxygen content above 10^{-6} wt. % and operating temperatures below 570°C [11, 12] are typically required for the formation of a stable passivating oxide in LBE. Therefore, at the elevated temperature of 700°C investigated in this study, continuous and protective passivation is not expected to occur for T91. This limitation incentivized previous papers [2, 13], which focused on the reducing environment. The oxygen level was between the equilibrium oxygen potential of Fe_3O_4 and FeCr_2O_4 at the testing temperature. It is found that the LBE penetrate into the T91 without following the GBs and the corrosion caused the martensite grains at surface transformed to ferrite grains. In those studies, no oxidising environment corrosion was studied.

Understanding the corrosion mechanisms of T91 under oxidizing conditions is crucial, since oxygen, which exists as an initial impurity in LBE and can also be introduced during operation[14], may also play a role in mitigating corrosion even at temperatures exceeding 600°C . According to the literature, under oxygen-saturated and oxygen-controlled conditions, the surface oxide typically consists of two layers: an outer magnetite (Fe_3O_4) layer and an inner Cr-containing layer, mainly composed of Fe–Cr–O spinel [15]. During the initial oxidation of fresh materials, variations in elemental diffusion and dissolution govern the formation, morphology, and stability of complex oxide structures, while the resulting oxide layers subsequently regulate further corrosion and dissolution processes [16, 17]. The growth of these layers

involves both the outward diffusion of elements from the steel (for example Fe, Cr, Si) and the inward migration of oxygen ions [18]. Cracks at the oxide/substrate interface have been reported in the literature. Dionisio et al. [18, 19], attributed these cracks to differences in the thermal expansion coefficients between the substrate and oxide scale, especially after long oxidation times. Considering the cyclic operating conditions of LBE-cooled reactors, such degradation could pose a serious concern for structural integrity.

Therefore, to improve the long-term reliability of structural materials in advanced LBE-cooled systems, investigating the corrosion behaviour of T91 under oxidising conditions (the oxygen level between the equilibrium oxygen potential of PbO and FeO at the testing temperature) at high temperatures is essential, which involves understanding the stability of oxide scales and identifying the mechanisms governing corrosion progression. While previous studies regarding the corrosion behaviour of steels in LBE in oxidising environment exist, most of them kept to lower temperatures (<600°C) and did not fully explore behaviour across orders of magnitude of time. We present a more systematic study across multiple timescales at higher temperatures, revealing both a mechanism for corrosion at these conditions and the critical conditions of providing protection through passivation.

2. Materials and Methods

2.1 Materials

T91, also known as Fe-9Cr-1Mo steel, is a ferritic/martensitic (F/M) steel with body-centred cubic (BCC) lattice structure. The materials used in this study was purchased from Edeltahl Witten-Krefeld GMBH in the quenched and tempered (Q&T) condition,

having undergone heat treatment in accordance with the manufacturer's specifications [20]. The final heat treatment of T91 is normalizing + high temperature tempering, the normalizing temperature is 1040°C, the holding time is not less than 10 minutes, the tempering temperature is 730-780°C, the holding time is not less than 1h, the structure after the final heat treatment is tempered fire martensite. This process ensures the desired mechanical properties, including a Brinell hardness range of approximately 190–248 HBW, making the alloy suitable for high-temperature structural applications. There is no further heat treatment done on the materials before corrosion test.

All the samples were cut from the same bar using wire electrical discharge machining (EDM) to dimensions of 25 mm x 25 mm x 3-4 mm. The composition from the alloy certificate is listed in Table 1.

Table 1: Composition of T91 material according to the alloy certificate provided by the manufacturer (wt. %).

Fe	Cr	Mo	Si	Mn	Ni	V	C	Nb	N	P	Al
89.0	8.76	0.93	0.34	0.50	0.30	0.20	0.09	0.07	0.05	0.02	0.01

The LBE used as in this study were obtained from Surepure Chemetals, Inc.. The original materials are ultra-high-purity lead (99.999 wt. %) and bismuth which are then combined in accordance with the eutectic composition of lead (44.5 wt. %) and bismuth (55.5 wt. %).

2.2 Corrosion tests

The samples were polished with successive SiC sandpaper grits (120, 240, 400, 800, 1600) with water lubricant and Buehler MetaDi diamond suspensions (9 μ m, 3 μ m, 1 μ m) adding three squirts of suspension every 20-30 seconds, concluding with a 50 nm alumina suspension to achieve a mirror finish on one side, while the opposite side was only ground with 120-grit SiC paper. The polishing wheel was run in the contra direction (samples and platen rotating in opposite directions) at 120 revolutions per minute (RPM), with 6 lbs. force per sample. They were then immersed in liquid LBE for 70, 245, or 506 hours at 700 °C. The oxygen level was between the equilibrium oxygen potential of Fe oxides and Pb/Bi oxides at the testing temperature [28]. The actual oxygen potentials of the cover gases were below the detection limit of the sensors used (0.1 ppm). Consequently, the measured concentrations of hydrogen and water vapour were used to estimate the oxygen partial pressures and concentrations, as a mass flow controller injected precise amounts of hydrogen, while the moisture meter was far more sensitive (1 ppb). Adding water vapor increased the oxygen concentration to provide an “oxidizing” atmosphere, while leaving water vapor out kept a “reducing” atmosphere inside the furnaces. A detailed description of the static corrosion experiments is provided elsewhere [21, 22].

After exposure, the samples were cut into four pieces, producing fresh, uncorroded surfaces. The pieces were mounted in Bakelite such that the fresh surfaces faced outward, while the LBE-corroded surfaces were embedded in the resin. The samples were subsequently ground and polished to reveal cross-sections comprising the uncorroded interior and the corroded surface layers. The cross-sections were then ground using the same procedure as for initial coupon preparation above, with the exception of using colloidal silica for final polishing instead of colloidal alumina. This

was done in order to provide a small degree of chemomechanical polishing and highlight grain contrast in optical and electron microscopy.

2.3 Characterisation methods

The morphology and chemical composition of cross-sections of the corroded samples were analysed using a Zeiss Merlin FEG-SEM equipped with a Bruker XFlash FlatQUAD 5060 F EDX detector and a Bruker e-flash high-resolution EBSD detector. EDX measurements were conducted at a working distance of 18 mm with an accelerating voltage ranging from 3 to 20 kV. Lowering the accelerating voltage increases both lateral and depth resolution in EDX mapping [23], which is particularly important for detecting oxygen ($K_{\alpha} = 0.523 \text{ keV}$), whose signal is prone to edge effects at higher voltages. Overlap with Cr ($L_{\alpha} = 0.573 \text{ keV}$) can occur at lower accelerating voltage, but this is addressed through peak deconvolution. Electron Backscatter Diffraction (EBSD) maps were acquired at a working distance of 18 mm, a sample tilt of 70° , a beam voltage of 20 kV, and a probe current of 5–10 nA. The data was processed using the Esprit 2.3 software.

Additional EDX analyses were performed using a dual-beam Zeiss Crossbeam 540 FIB-SEM equipped with the Oxford Instruments XMax^N 150 EDX detector and Nordlys Max EBSD system. Measurements were conducted at a working distance of 5 mm, with an accelerating voltage of 5–30 kV and a probe current of 2 nA. The data were processed by Aztec 5.1 software. For verification, higher accelerating voltages were employed to resolve potential overlaps, such as those between Mo ($L_{\alpha} = 2.293 \text{ keV}$) and Pb ($M = 2.342 \text{ keV}$) peaks.

3. Results

3.1 Differences in observed corrosion patterns

Corrosion is a complex process influenced by several microstructural factors, including surface condition, grain orientation, and grain boundary distribution among other factors [24]. Its manifestation can vary with exposure duration (70 h, 245 h, and 506 h in this study) as well as spatially across a single specimen. Fig. 1 shows representative corrosion morphologies observed by SEM with voltage of 5-20 kV with secondary electron (SE) detector after different exposure times. Based on the SEM observations, three types of corrosion patterns were identified. The presented morphologies are used only to illustrate the characteristic corrosion features and are not necessarily taken from the deepest corroded regions. Therefore, these images should not be used to compare the severity of corrosion among the samples.

1. **Intergranular internal corrosion** — This type occurs preferentially along grain boundaries (GBs). As shown in Fig. 1(a) and (b), the corrosion happens mainly in the GBs. The differences are that as shown in Fig. 1(a), oxidation occurs along much finer GBs in the 70 h exposure sample, whereas in the 245 h sample (Fig. 1(b)), oxidation extends predominantly along larger GBs which can be prior austenite grain boundaries (PAGBs) or GBs of the recrystallized grains, which will be discussed following. The SEM images for Fig. 1(a) with larger magnification is shown in Supplementary materials (S1). In Fig. 2(a), also presented a larger scale SEM image of 70 h corroded sample. Fig. 1(c) shows the spot where initialization of one such intergranular corrosion is observed from the specimen exposed to LBE for 506 h.

2. **Wider area corrosion** — In some regions (Fig. 1(d)–(f)), corrosion extends beyond GBs into the grain interiors. These regions appear sporadically and may represent an advanced stage of intergranular corrosion, in which corrosion initiates at grain boundaries and extends into adjacent grains, forming wider corroded areas. The red arrows in Fig. 1(f) indicate cracks may form as a consequence of the mismatch in thermal expansion coefficients between the substrate and the oxide scale [18]. These cracks become more frequent with increasing exposure time. From SEM imaging alone, it is difficult to distinguish whether these features result from liquid metal (LBE) penetration or the formation of large oxide structures. To clarify their origin, EDX analysis was performed to assess elemental redistribution within these zones.

3. **Unaffected regions** — In all three exposure-time specimens, certain areas exhibit little to no visible corrosion, indicating local variations in corrosion susceptibility. These regions may be relevant to discussions on the potential for passivation at elevated temperatures (>600 °C). As mentioned earlier, passivation at these conditions may not be complete, but it may form local areas of passivation which resist both liquid metal wetting and further oxygen ingress or iron leaching.

For the 70 h corroded sample, most surface shows the corrosion with morphology of Fig. 1(a) with some place shows wider area corrosion shown in Fig. 1(d) and well-protected region in Fig. 1(g). For the 245 h corroded sample, the corrosion pattern shows in Fig. 1(b) and the wider area corrosion shows in Fig. 1(h) are the main corrosion morphology. Little areas are well-protected and show no corrosion. For the

506 h corroded sample, the corrosion mainly appears as the wider area corrosion shows in Fig. 1(f) and much less region shows intergranular corrosion or no corrosion. This suggests a possible corrosion process which can be discussed in two forms according to effective protection layer formed or not on the surface.

- 1) First, for the area where there is no effective protection layer formed. Oxygen diffuses into the GBs which can be treated as fast diffusion path and form GBs corrosion as shown in Fig. 1(a). Then, with longer duration time, it can develop to wider area corrosion as shown in Fig. 1(d)-(f).
- 2) Secondly, the areas are well protected with a continuous oxide layer as shown in Fig. 1(g)-(i). After longer duration time, will be slowly corroded and form the larger GBs corrosion shown in Fig. 1(b) and small intergranular internal corrosion shown in Fig. 1(c). These can further develop to wider area corrosion as shown in Fig. 1(e)-(f).

To further understand the corrosion mechanism, EDX and EBSD are conducted on these samples to verify the mechanism proposed above and to elucidate whether local regions of elemental depletion/enrichment, or orientation relationships, correlate strongly with any observed features.

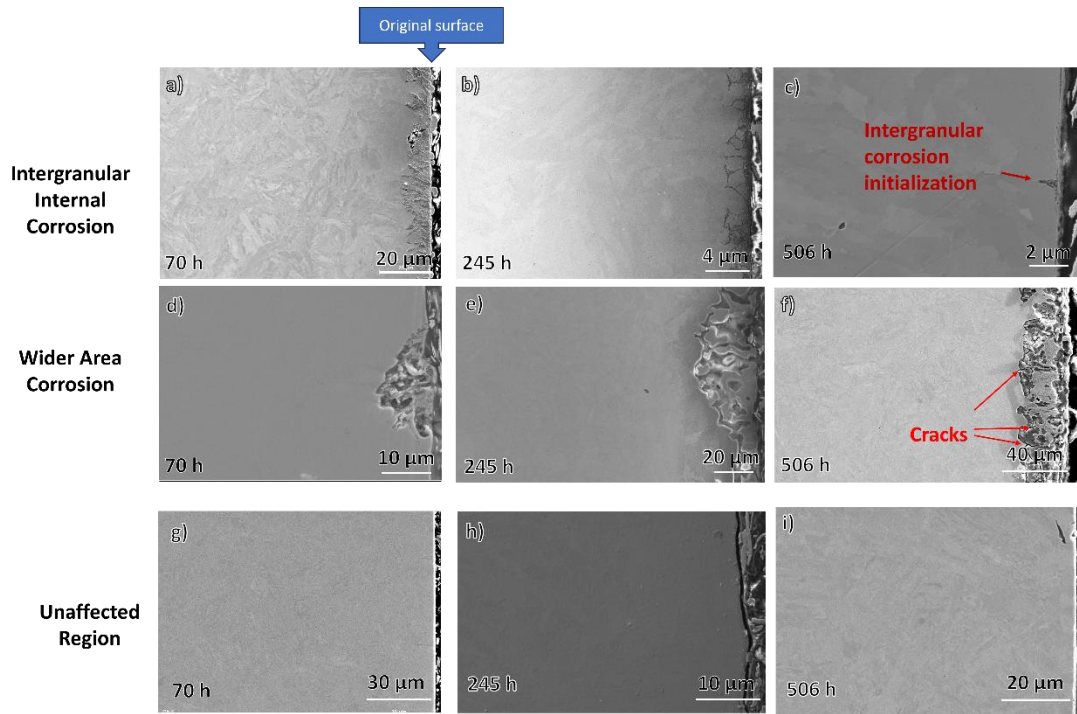


Fig. 1. Different kinds of corrosion patterns for 70 h, 245 h, and 506 h corroded samples in oxidising environment at 700°C, respectively. (a) (b) (c) Intergranular corrosion with one intergranular corrosion initialization marked in (c). (d) (e) (f) Area corrosion with the cracks marked in (f). (g) (h) (i) (l) Unaffected regions.

3.2 Intergranular internal corrosion

Fig. 1(a) and Fig. 1(b) shows two different kinds of intergranular internal corrosion, one presumably following much finer GBs presumably martensite GBs and the other following much larger GBs. To study the mechanism that causes the difference, EDX and EBSD are used.

3.2.1 Intergranular corrosion at martensite GBs

Fig. 2 shows SEM-EDX results of the sample corroded for 70 h. From Fig. 2 (a), intergranular internal corrosion following martensite GBs can be observed, accompanied by the formation of a surface layer over the original material. To

elucidate whether regions of differing elemental concentration correlate with these features, EDX measurements were performed at 5 kV and 2 nA [23] – the low accelerating voltage localized the EDX information to the top 2-3 μ m of material [25]. The EDX results in Figs. 2(b)–(d) captured from the blue dashed rectangular in Fig. 2(a) show that the corroded GBs contain mainly Cr oxides, with minor Si oxide formation. Although thermodynamic studies indicate that Si oxides form more readily than Fe–Cr–O oxides [21], the relatively low Si content in T91 (0.34 wt. %) compared with Cr (8.76 wt. %) suggests that Cr oxidation is predominant.

The dense layer formed on the T91 surface consists primarily of Fe, with negligible Cr, Si, or O detected. As shown in Fig. 2(f), no Pb was detected in this region. To quantitatively assess the observed compositional variations, an EDX line scan was performed along the white line indicated in Fig. 2(a), with the results shown in Fig. 2(g). Three distinct regions were identified:

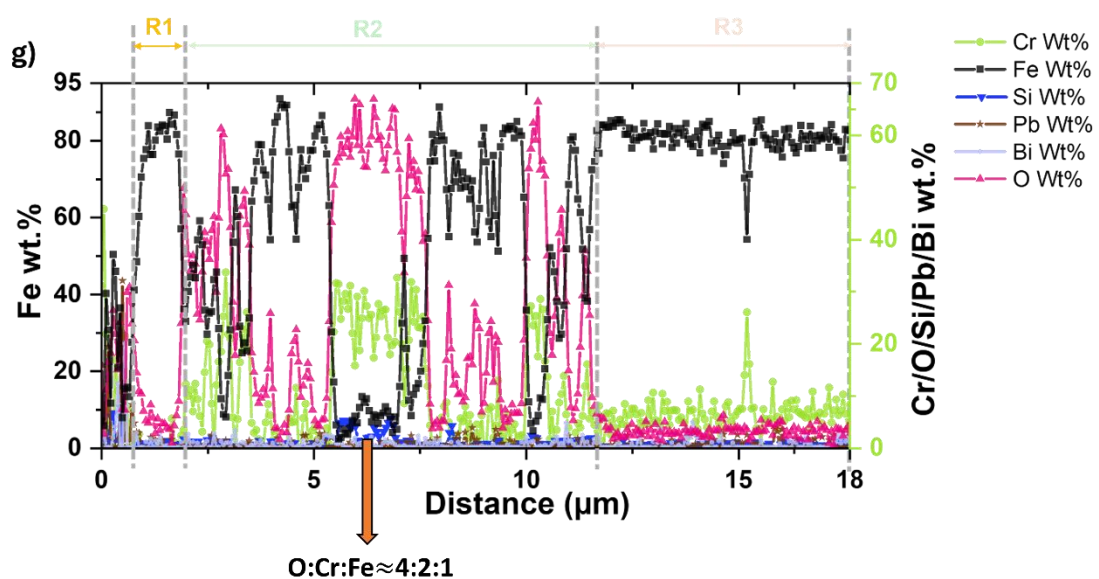
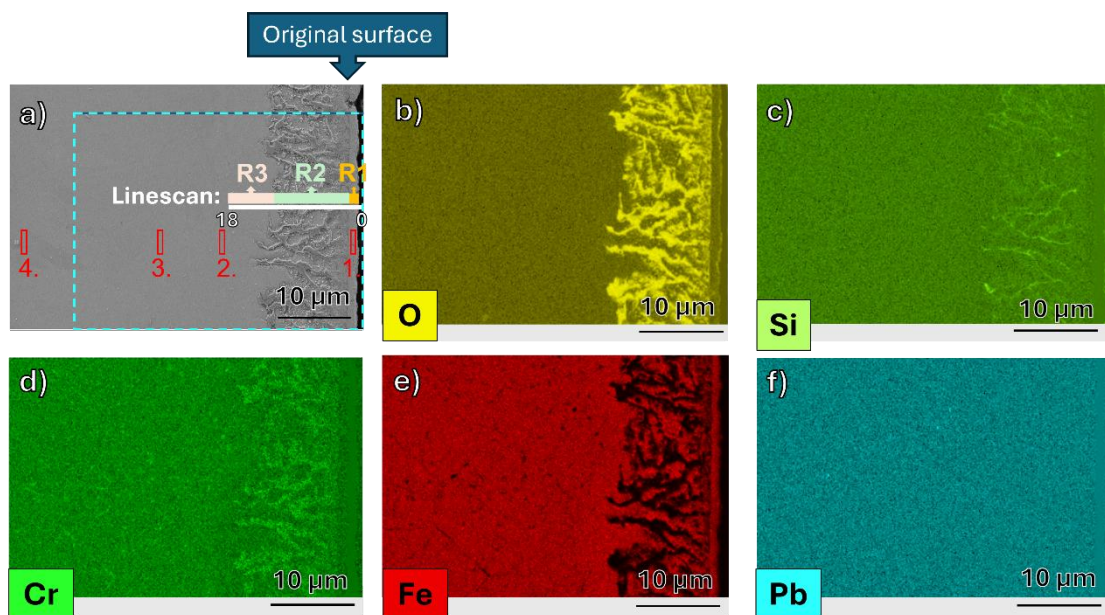
Region 1: an Fe-enriched surface layer.

Region 2: oxidised grain boundaries.

Region 3: the unaffected T91 matrix.

According to Fig. 2(g), Region 1 is predominantly Fe (>80 wt. %), with only minor amounts of other elements. To further compare the compositional features, spectra were extracted from four areas marked by red rectangles in Fig. 2(a), as shown in Fig. 2(h). The presence of C is likely due to surface contamination during prolonged EDX exposure. Nevertheless, the spectrum of the Fe-enriched surface layer from Spectrum 1 is very similar with Spectra 2 and 3, confirm that these areas consist mainly of Fe. The oxygen content in Spectrum 1 is too low to classify it as an Fe oxide.

Spectrum 4 exhibits a higher Cr concentration than Spectra 2 and 3, likely due to Cr depletion in the surrounding matrix caused by the formation of Cr-rich oxides in GBs. Region 2 is characterised by oxides composed primarily of Cr, O, and Fe, with minor Si enrichment. The elemental ratio of O:Cr:Fe \approx 4:2:1 is consistent with the stoichiometry of chromite-type spinel oxides reported in the literature [26, 27]. Region 3 represents the unaffected substrate, corresponding to the as-received T91 microstructure.



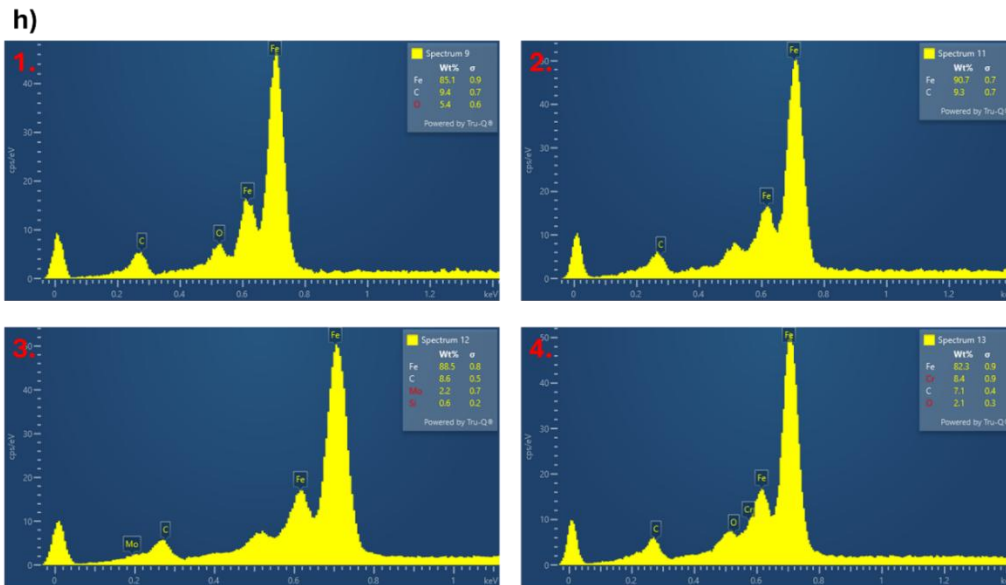


Fig. 2. SEM-EDX [Sample: 70 h, oxidising environment, 700 °C, LBE]. (a) SEM image with the linescan position highlighted with the white line. The different regions of the linescan are highlighted with R1 in orange, R2 in green, and R3 in pink. The positions from where the spectra of Fig. 2 (h) were acquired (S1-4) are highlighted with the four red rectangles. (b)-(f) EDX results highlight O, Si, Cr, Fe, and Pb from blue dashed rectangular in Fig. 2(a). (g) EDX linescan follows the position of Fig. 2 (a) with R1, R2, and R3 marked. (h) Spectra from the positions highlighted in Fig. 2 (a) with red rectangles.

While EDX analysis provides only compositional information, determining which phase(s) exist requires knowledge of the lattice structure. Therefore, EBSD measurements were performed in a region corresponding to that shown in Fig. 2, and the results are presented in Fig. 3. The Fe-enriched surface layer is indicated by a dashed rectangle in Fig. 3(a). As shown in Fig. 3(b), the indexed lattice structure of this layer is body-centred cubic (BCC), identical to that of the T91 matrix. Many researchers

reported Fe oxides formed outside chromite-type spinel oxides [26, 27]. However, FeO ($Fm\bar{3}m$ space group, No. 225) and Fe_3O_4 ($Fd\bar{3}m$ space group, No. 227) are both face-centred cubic (FCC) phases. Combining this crystallographic information with our EDX results indicates that the surface layer is composed of a ferritic steel rather than an oxide. This differs from previous reports, which commonly identified the surface layer as Fe_3O_4 [28, 29]. This BCC layer is spatially heterogeneous and discontinuous across the specimens examined, thus more representative data are shown in *Supplementary Materials S2 and S3* to fully document this surprising finding.

Fig. 3(c) further shows that the average grain misorientation within the oxidised GBs and the Fe-enriched surface layer is lower than that in the underlying T91 matrix, suggesting microstructural relaxation during corrosion. This is well known to occur, as selective dissolution of elements allows reorganization and recrystallization of new phases which will largely reduce the grain misorientation. For example, Cairang et al [30-32]. recently reported ferritization of 316 stainless steel corroding in Pb-4Bi under similar conditions. Additional results are shown in *Supplementary Materials S2 and S3* which can further confirm the representativeness of the morphology observed above.

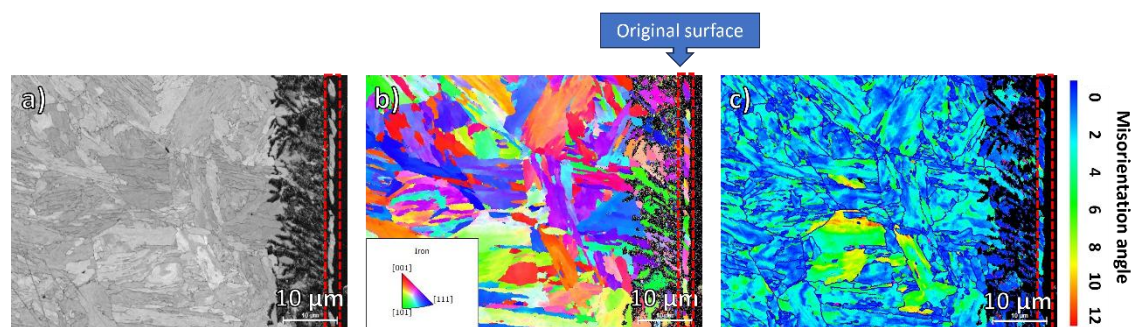


Fig. 3. SEM-EBSD results highlighting the surface formed Fe-enriched layer with dashed rectangular [Sample: 70 h, oxidising environment, 700 °C, LBE]. (a) SEM image

corresponding to EBSD maps. (b) EBSD-IPFZ map. (c) EBSD grain average misorientation map.

After a prolonged exposure of 506 h, corrosion continues to propagate preferentially along martensitic GBs. However, the extended duration allows for further elemental diffusion, leading to compositional variations in the GB oxides, as shown in Fig. 4. It is important to note that the contrast in this EDX maps is independent for each element; therefore, the brightness of a given element (e.g., Si) does not indicate its relative concentration compared with other elements or regions. All EDX maps have been corrected for background noise but not normalized, meaning the intensity scales for different elements are not adjusted to sum to 100%.

Fig. 4(a) shows a discontinuous, Fe-enriched layer formed outside the original surface, similar to those observed in Figs. 2(a) and 3(a). Fig. 4(b) and 4(c) reveal that Cr and Si are enriched along the GBs. The EDX line scan conducted along the line indicated in Fig. 4(b) and 4(c), with results shown in Fig. 4(e), demonstrates that Cr-rich and Si-rich oxides appear in an alternating pattern along the corroded boundary—distinct from the distribution observed in the 70 h corroded sample. This difference likely arises because the prolonged exposure allows Si to diffuse more extensively toward the corroded GBs. The corresponding IPFZ map of the corroded region is presented in Fig. 4(d). Much lower accelerating voltage is needed to visualize the oxygen signal, the results can be found in *Supplementary Materials S4* which shows that oxygen appears in the same location with Cr.

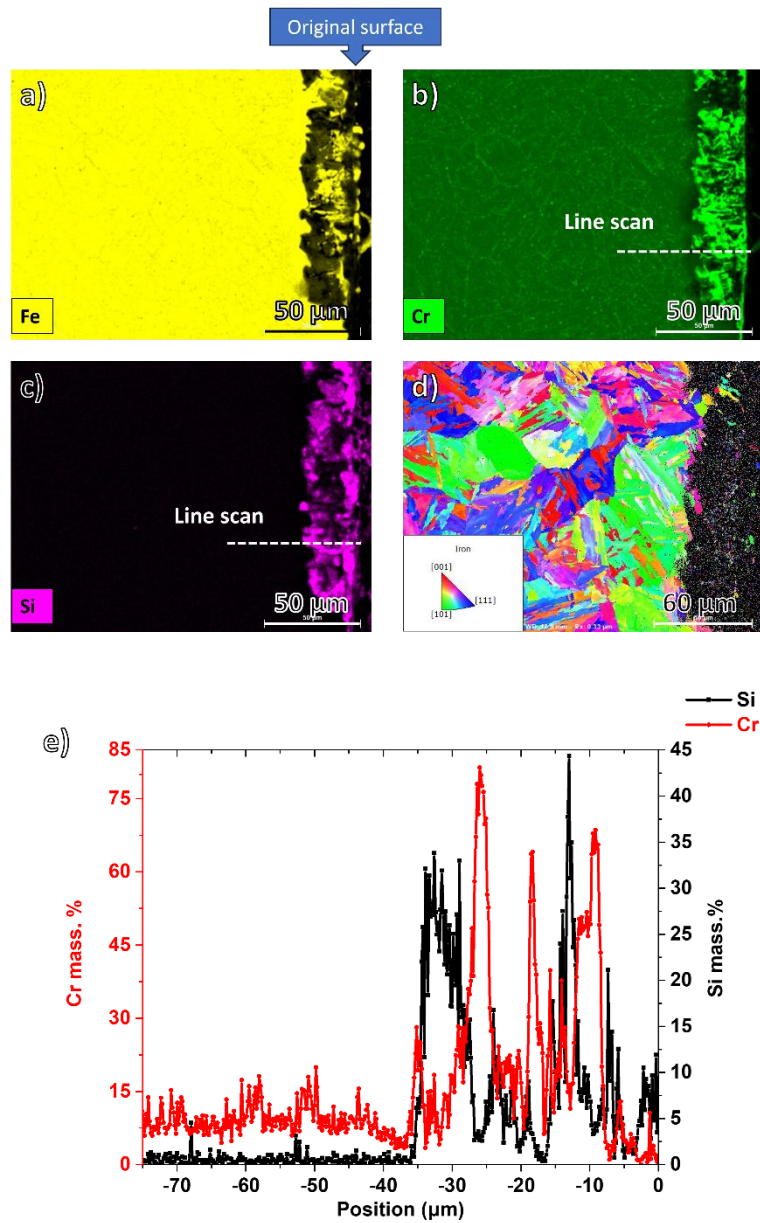


Fig. 4. SEM-EDX and EBSD with oxidised GB [Sample: 506 h, oxidising environment, 700 °C, LBE]. (a) EDX map highlighting Fe. (b) EDX map highlighting Cr. (c) EDX map highlighting Si. (d) EBSD-IPFZ map. (e) EDX line scan result following the line shown in Fig. 4 (b) and (c) with the original sample surface as position 0 μm.

3.2.2 Intergranular internal corrosion at larger GBs

As it shows in Fig. 1, the 245 h corroded sample in Fig. 1 (b) shows a intergranular internal corrosion following larger GBs compared to Fig. 1(a). To further reveal the chemical composition information of the 245 h corroded sample, low energy (5 keV) EDX was used to acquire the O signal at higher spatial resolution [23]. The results are shown in Fig. 5. Combining the results shown in Fig. 5(b)-(d), it is seen that the oxidised GBs consist of Cr and Si oxides. An obvious Cr-depleted zone is observed in Fig. 5(b) highlighted by a yellow dashed box. The Cr-enriched precipitates observed in the left side unaffected region dissociated in the highlighted Cr-depleted region. This is probably because the Cr diffused from the matrix to the oxidised GBs and oxide protection layer on the surface and left a Cr-depleted region surrounding them. The larger depletion Cr layer was not observed in 70 h and 506 h corroded sample which may induce these larger corroded GBs.

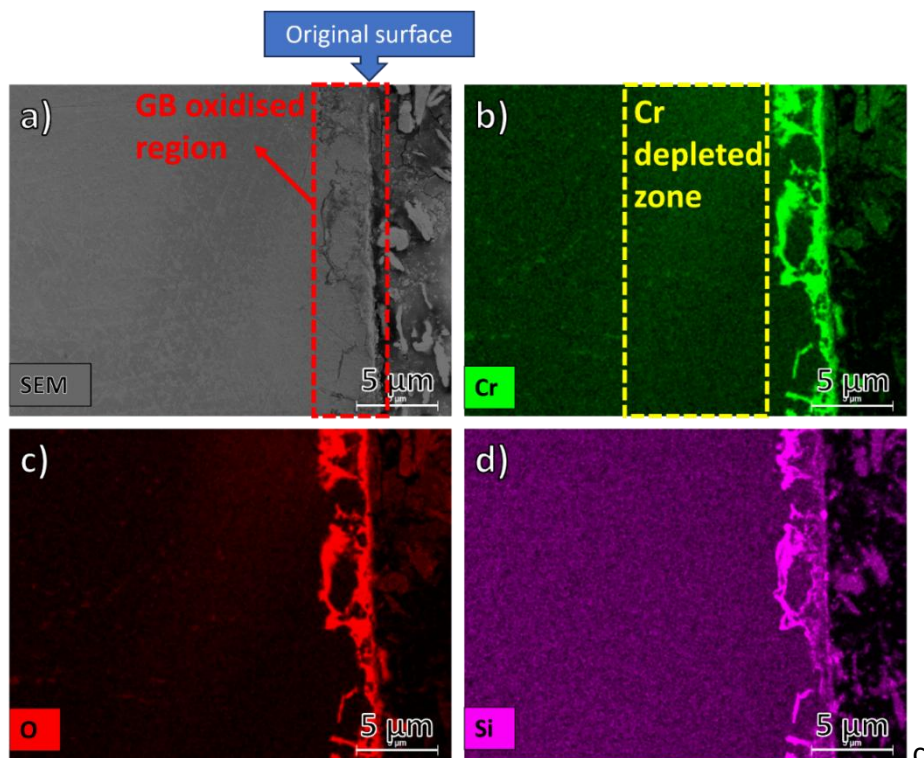


Fig. 5. Low energy SEM-EDX results [Sample: 245 h, oxidising environment, 700 °C, LBE].

(a) SEM image with a red dashed box highlighting the GB oxidised region. (b) EDX result highlighting the Cr with the yellow dashed box showing the Cr depleted zone. (c) EDX result highlighting O. (d) EDX result highlighting Si.

Fig. 6 shows EBSD results corresponding to the region shown in Fig. 5(a), but at a lower magnification. By comparing the scale bars of Fig. 5(a) and Fig. 6(a), it can be seen that the grain boundary–corroded area, outlined by the red dashed rectangle in Fig. 6(a), is clearly identifiable. In addition, the adjacent region, marked by the yellow dashed rectangle, exhibits a distinct grain morphology compared with the unaffected matrix. As shown in Fig. 6(b) and (c), the areas highlighted by the red and yellow dashed rectangles display a transformation from martensitic laths to more equiaxed grains with lower grain-averaged misorientation. This observation suggests that martensitic decomposition has occurred in these regions.

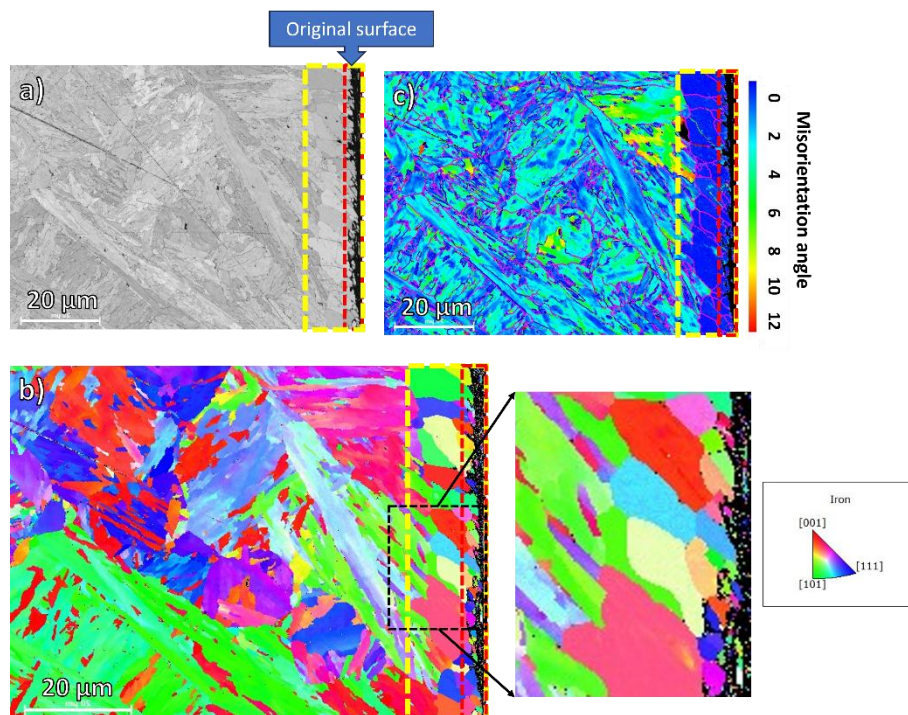


Fig. 6. SEM-EBSD results highlighting the phase-changed region in the yellow dashed box, and the GB oxidised region in the red dashed box, corresponding to areas shown in Fig. 5 [Sample: 245 h, oxidising environment, 700 °C, LBE]. (a) SEM result (Secondary Electron). (b) EBSD IPFZ map with the local region zoomed in for the black dashed box. (c) Grain average misorientation with scale bar.

To quantify elemental distributions in the corroded GBs of 245 h corroded sample, a EDX line scan was conducted through the GBs as shown in Fig. 7(a). Fig. 7(b) shows the corresponding changes in elemental concentrations of Cr, Fe, Mo, Si, and O. From the free surface to unaffected matrix, an Fe oxide, Fe-Cr oxide, and Si oxide can be observed. By analysing changes in the Cr content, a Cr depletion zone can be seen near the Cr-enriched oxides. There are also Mo-enriched precipitates observed near the corroded GBs. As the Pb-M x-ray energy is 2.342 keV and the Bi-M x-ray energy is 2.419 keV, similar to the Mo-L α energy of 2.293 keV. This raises concerns of peaks overlapping, thus a higher voltage of 30 keV is used at the expense of some spatial resolution, and the result shows that the precipitates are Mo-enriched (*Supplementary Materials S5*).

From Fig. 7(c), the Si-enriched and Cr-enriched oxides appear in different places, suggesting the formation of layered oxides in the GBs. This is similar with what we observed in the 506 h corroded sample, and is shown in Fig. 4(e).

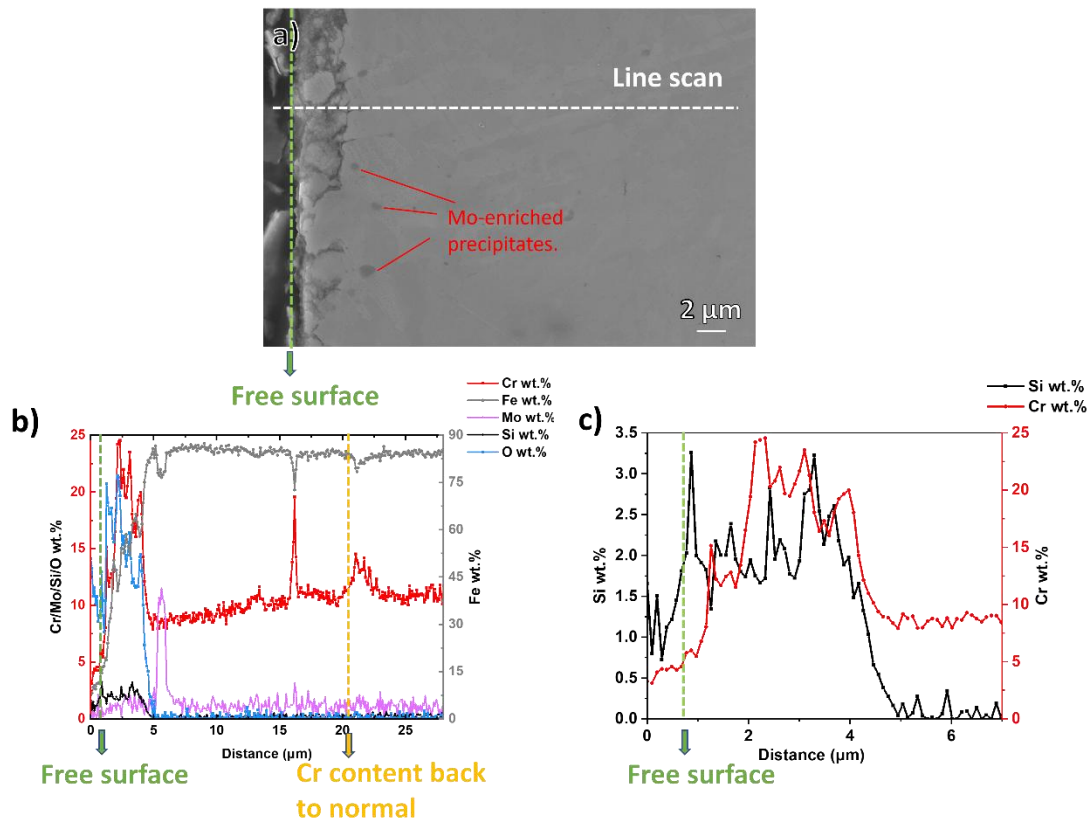


Fig. 7. SEM-EDX line scan results for 245 h corroded sample in oxidising environment. (a) SEM SE image showing the position of the line scan and Mo-enriched precipitates. (b) EDX line scan result showing content of Cr, Fe, Mo, Si, and O. (c) EDX line scan showing Si and Cr content at the surface region.

Cracks resulting from the mismatch in thermal expansion coefficients between the substrate and the oxide scale are also observed in the samples corroded for 245 h and 506 h. This is likely due to prolonged oxidation, which promotes crack formation [18]. As shown in Fig. 8, intergranular corrosion along GBs can be observed in the regions highlighted by the black dashed boxes. Fig. 8(f) further reveals that Pb penetrates through these cracks, enabling its rapid diffusion into the deeper layers of the material and thereby exacerbating corrosion. Moreover, corrosion-induced cracking can

significantly reduce the mechanical strength of the material and may lead to oxide spallation within the circulation system, potentially resulting in blockage. The cracks observed in the 506 h corroded sample can be found in *Supplementary Materials S6*.

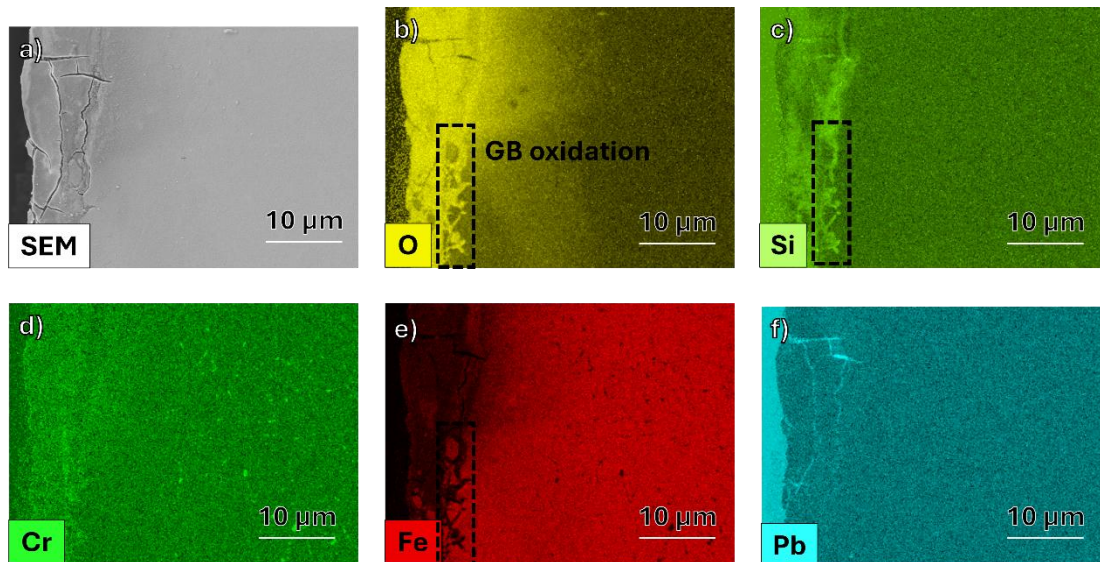


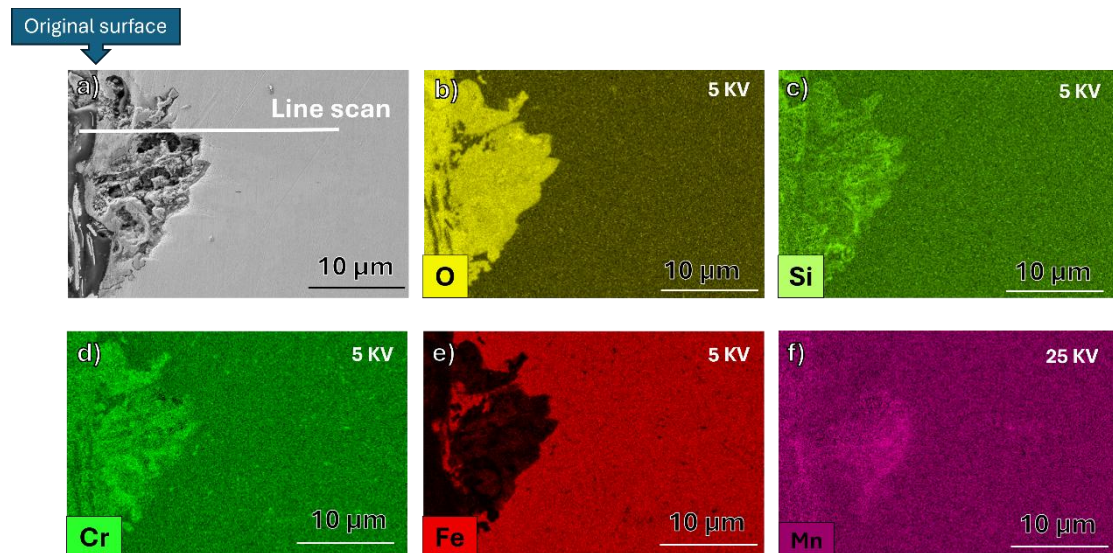
Fig. 8. SEM-EDX with cracks observed in the oxide layer [Sample: 245 h, oxidising environment, 700 °C, LBE]. (a) SEM image. (b)-(f) EDX results highlight O, Si, Fe, Cr, and Pb, respectively, with GB oxidation highlighted.

3.3 Wider area corrosion

As discussed in Fig. 1, GB corrosion will eventually develop to larger area corrosion, extending beyond the original GB regions. However, even in this wider area corrosion, there is a development process. Fig. 9 shows the initial stage of wider area corrosion following GB corrosion. EDX results shown in Fig. 9 were obtained at 5 kV in order to significantly improve spatial resolution and provide oxygen signal. The analysis confirms that the major corrosion products are oxides, with only trace amounts of LBE detected. Fig. 9(b)-(d) reveal the distribution of Cr- and Si-enriched oxides. In Fig. 9(e),

There is an Fe depletion in the corroded region with only small amount left. Furthermore, Fig. 9(f) shows the distribution of Mn, which acquired with an accelerating voltage of 25 kV. As with 5kV, there will be the issue of Pb and Mn overlapping issue as discussed before. *Supplementary Material S6* shows the EDX results for other elements at 25 kV. *Supplementary Material S7* also shows the EBSD results for this region.

To quantify the elemental composition and assess the extent of LBE penetration, an EDX line scan was performed along the white line indicated in Fig. 9(a), with the corresponding results presented in Fig. 9(g). The Fe signal is depleted within the oxidized GBs, while Cr oxides dominate the corrosion products. The multiple Cr peaks suggest the formation of layered, chromite-type spinel oxides. Si shows only minor enrichment, and minimal LBE penetration is observed.



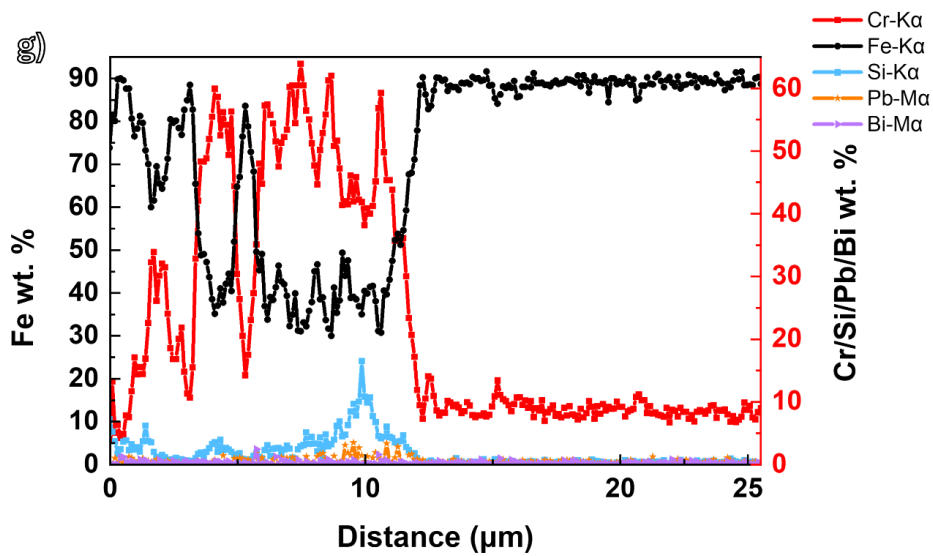


Fig. 9. SEM-EDX results acquired at 5 kV in regions of wider area corrosion [Sample: 70 h, oxidising environment, 700 °C, LBE]. (a) SEM image for Fig. 7.1 (d). (b)-(f) SEM-EDX results highlighting O, Si, Cr, Fe and Pb, respectively. (g) EDX line scan result for the white line in Fig. 9 (a).

The second stage of wider area corrosion occurs after oxide formation, when the oxide layer detaches from the surface, allowing LBE to further penetrate into the material. Fig. 10 shows one such region exhibiting more severe LBE penetration. Fig. 10(d) and (e) reveal that corrosion at this stage is dominated by LBE intrusion, characterised by high concentrations of Pb and Bi. This may account for the low Cr content observed in Fig. 10(b), as LBE likely dissolves the surrounding Cr during penetration due to its relatively higher solubility compared to other alloying elements in T91. Fig. 10(c) shows Si enrichment around the LBE intrusions, where Si-enriched oxides form adjacent to LBE-rich regions, with almost no chromite-type spinel oxides nearby.

suggests that Si-enriched oxides possess higher resistance to LBE corrosion than other oxides.

To further clarify the elemental distribution, a line scan was performed along the white line indicated in Fig. 10(a), and the corresponding results are shown in Fig. 10(g). Cr dissolution is evident within the Pb- and Bi-enriched regions, and a Cr-depleted zone extending from approximately 5 μ m to 10 μ m can be identified. Due to its eutectic properties, LBE separates into two phases at room temperature [2]. The line scan in Fig. 10(g) and the EDX map in Fig. 10(b) both reveal a discontinuous Cr-enriched oxide layer at the surface, which appears insufficient to hinder further LBE penetration. Additionally, Fig. 10(g) shows an Fe-enriched surface layer, likely formed through outward Fe diffusion and recrystallisation which can be seen in Fig. 10(f), 245 h corroded samples show similar results and can be found in *Supplementary Materials S8*.

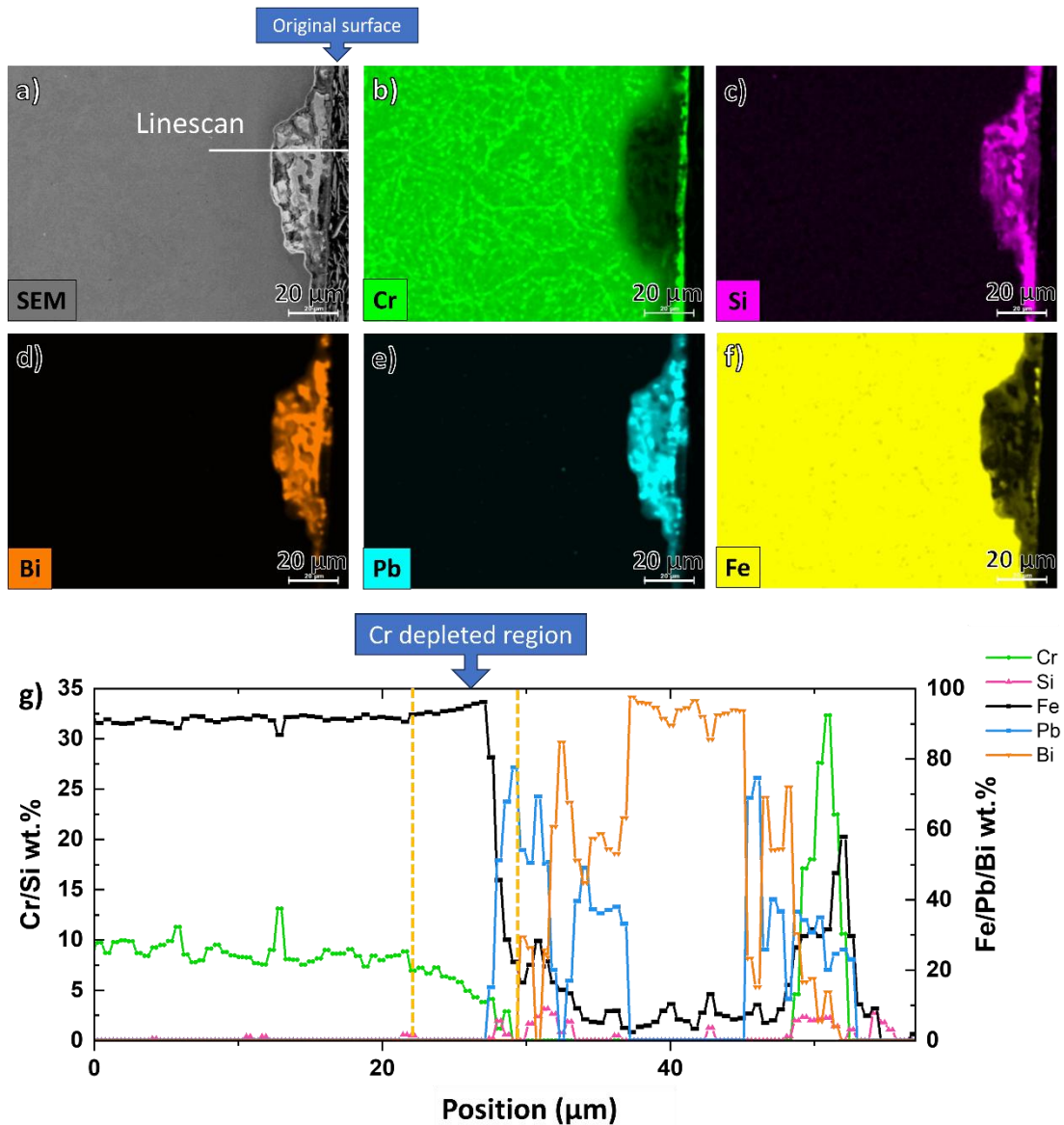


Fig. 10. SEM-EDX and EBSD results acquired at 20 kV [Sample: 245 h, oxidising environment, 700 °C, LBE]. (a) SEM view indicating the position of the EDX line scan of Fig. 10(g) highlighted with the white line. (b) (c) (d) (e) SEM-EDX results highlighting Cr, Si, Bi, and Pb, respectively. (f) SEM-EBSD IPFZ map. (g) Line-scan result for the white line in Fig. 10(a).

3.4 Regions unaffected by corrosion

All the samples contain regions showing no apparent signs of corrosion, as illustrated in Fig. 1(g)–(i). Studying these unaffected areas is crucial, as they may provide insights into how passivation can be used to enhance the corrosion resistance of T91 steel. Fig. 11 presents SEM–EDX and EBSD results for the sample corroded for 506 h. No obvious corrosion can be observed in Fig. 11(a), and lack of Fe depletion in Fig. 11(d) further confirms this. From Fig. 11(b) and (c), it can be inferred that the formation of a Cr- and Si-enriched surface layer effectively protected the underlying material. A Cr-depleted region is observed adjacent to the oxide layer, and the corresponding EBSD results shown in Fig. 11(e) and (f) reveal more equiaxed grains in this area, accompanied by a significantly lower grain-averaged misorientation. The Cr depletion may have induced martensitic decomposition in this region. The 245 h corroded sample shows a similar result, and can be found in *Supplementary Materials S9*.

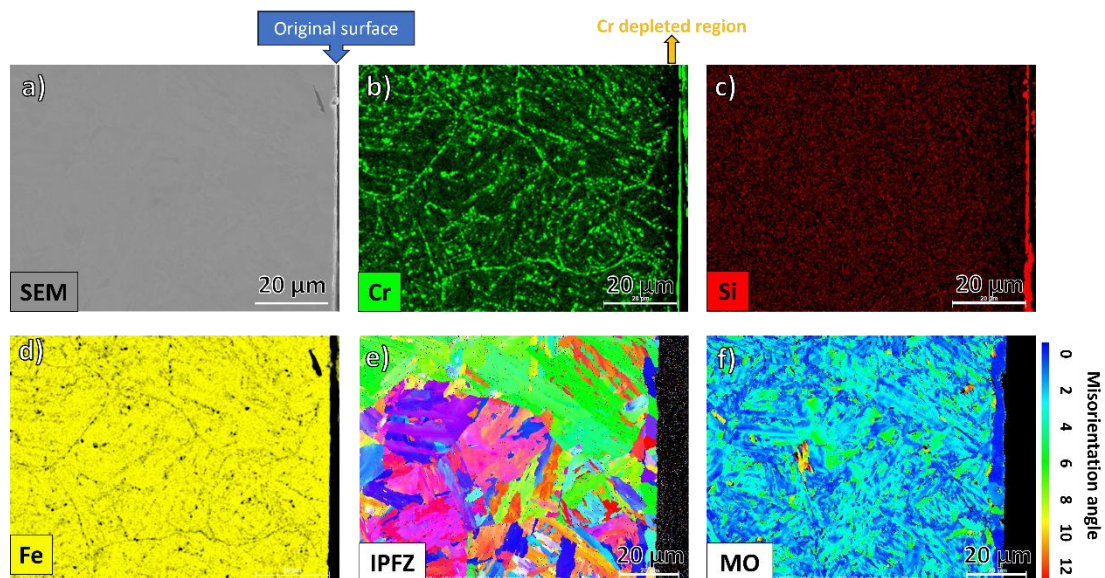


Fig. 11. SEM-EDX and EBSD results for one representative area with no obvious corrosion [Sample: 506 h, oxidising environment, 700 °C, LBE]. (a) SEM SE view. (b)

SEM-EDX result highlighting the Cr with the Cr depleted region marked. (c) SEM-EDX result highlighting Si. (d) SEM-EDX result highlighting Fe. (e) SEM-EBSD IPFZ map. (f) SEM-EBSD grain average misorientation (MO) with scale bar.

Fig. 12 exhibits minimal corrosion as Fig. 11. Even so, subtle phase changes are visible in Fig. 12(d–e). A direct comparison of Fig. 11(b) and Fig. 12(b) shows that the former contains a substantially larger Cr-depleted region, aligning with the more extensive microstructural transformation observed.

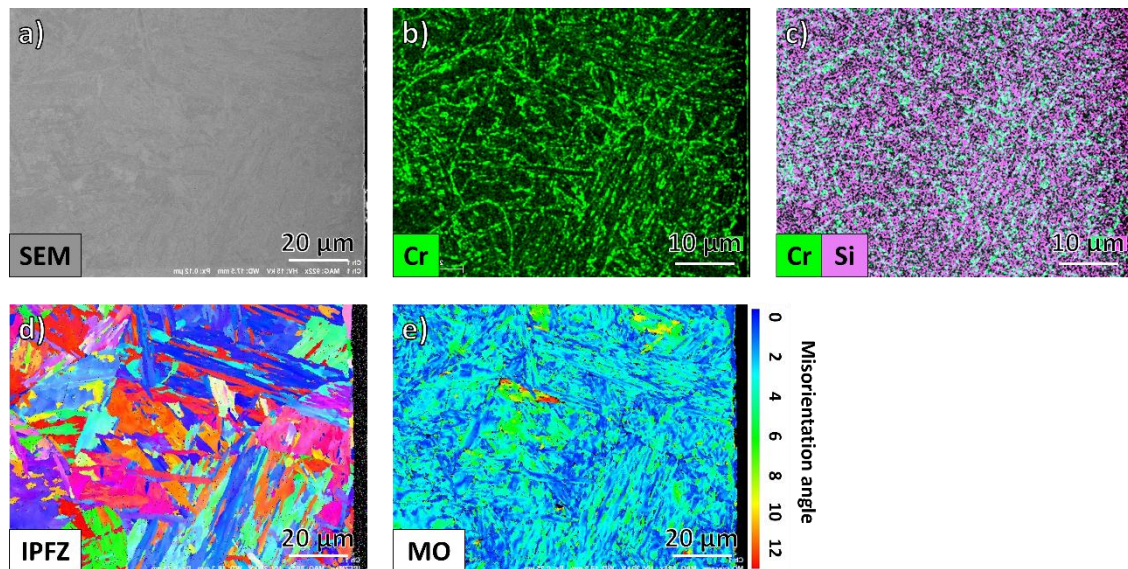


Fig. 12 SEM-EDX and EBSD results for one representative area with no obvious corrosion in SEM view [Sample: 506 h, oxidising environment, 700 °C, LBE]. (a) SEM view. (b) SEM-EDX result highlighting the Cr. (c) SEM-EDX result highlighting Cr and Si. (d) SEM-EBSD IPFZ map. (e) SEM-EBSD grain average misorientation with scale bar.

4. Discussion

In this study, oxidized samples with different exposure time were analyzed. The oxides located at different positions of the oxide film have been examined in detail by multiple characterization techniques. To understand the evolution of chemical composition and crystallographic information of the oxides, EDX and EBSD were used. Intergranular internal oxidation, wider area corrosion, and no obvious corrosion areas were observed. Within the GB oxidation, we observed 2 forms of products, one is the Fe/steel BCC layer and one is the Cr/Si enriched discontinuous layer. The wider area corrosion shows extensive oxide formation in some region and LBE penetration observed in some cases. In the none obvious corroded region, a dense Cr/Si oxide layer is observed. Based on the results presented above and in literature, the detailed formation mechanisms of the different oxide layers are proposed and discussed below.

4.1 Formation of GB oxides

There are many literatures researching the oxides layers formed on F/M steels after exposure to high temperature mediums, such as steam [26, 27], carbon dioxide [33], and liquid Pb or LBE [34, 35]. In the papers mentioned above, they all proposed the oxide formation and growing mechanisms for outer layer which growing outside the original surface, and inner layer (inside the original steel surface). The oxidation behaviour of T91 steel is governed by elements diffusion (both elements in T91 and LBE). At the T91 and liquid LBE interface, there are 2 possible diffusion paths: (a) elements from T91 diffuse outwards to liquid LBE and form oxides; (2) oxygen diffuse inwards from liquid LBE to T91 to form oxides.

The oxygen content fluctuation in Fig. 2(g) suggests the diffusion of oxygen in the T91. Thus, for oxygen, it is more as an inward diffusion process. This is shown in the literatures many times [34, 35]. The markedly more negative Gibbs free energies of formation for Cr_2O_3 and SiO_2 compared to Fe-oxide phases drive the preferential oxidation of Cr and Si [36-38]. According to the results reported in the literature [26, 39, 40], with the increase of environmental oxygen partial pressure, the formation of different types of oxides in Fe-Cr steels follows the sequence of Cr_2O_3 , FeCr_2O_4 , Fe_3O_4 , and Fe_2O_3 . As a result, oxygen diffusing inward reacts primarily with these solutes, leading to the formation of dispersed Cr and Si enriched oxides and Fe-Cr-O spinel-type oxides within the alloy.

However, in the literatures mentioned above [26, 27, 33-35], they all claim that oxygen diffusion is the main factor controls the Cr-enriched oxide formation as the Cr content measured in oxide keeps the same as it the unaffected matrix. This is very different to what we overserved in Fig. 2(g), Fig. 4(e), Fig. 9(g), and Fig. 10(g). A much higher Cr content is observed in oxidised GBs compared to the unaffected matrix. The key difference is the test temperatures they used are $<600\text{ }^\circ\text{C}$ and we are using $700\text{ }^\circ\text{C}$ for the samples shown in this study. A higher temperature may allow Cr to diffuse from surrounding to the corroded GBs. Ye's research at 823 K also shows a Cr enriched zone in oxides and Cr depleted zone around [41]. Chen's study at $790\text{ }^\circ\text{C}$ also shows the Cr enrichment in the oxide area [27]. Thus, it is possible that Cr will also diffuse during the oxidation process.

To conclude, at higher temperature, the diffusion of metal elements and oxygen both control the corrosion process.

4.2 Fe-rich layer on surface

In the literature, the formation of outer oxide layer and the formation mechanism has been widely discussed [27, 34, 35]. It is widely believed that the formation of the outer oxide layer is due to the outward diffusion of Fe from the inner oxide layers [26]. Once the F-M steels are exposed to the high-temperature coolant (water, steam, liquid metal...), Fe from the inner oxide layers diffuses out and reacts with the oxygen at the outmost of the surface oxide film, forming an Fe dominated oxide layer [27]. There are different kinds of outer oxide layers observed in literatures, the most common ones are Fe_2O_3 and Fe_3O_4 . The oxygen partial pressure is accounted for the formation of different oxides. High oxygen partial pressure favours the formation of Fe_2O_3 while the lower ones will lead to the formation of Fe_3O_4 [42, 43].

However, in our study, the outer layer observed in the 70 h corroded sample mainly consists of Fe (over 80 wt. %) and exhibits a BCC lattice structure, as shown in Figs. 2 and 3. Since Fe_2O_3 possess hexagonal structure, and $\text{Fe}_3\text{O}_4/\text{FeO}$ are both FCC structure, and no new phases are observed in the EBSD phase map, the outer layer shown in Figs. 2 and 3 cannot be attributed to either Fe_2O_3 or Fe_3O_4 . Instead, it is more likely to be a ferritic steel phase with a high Fe content. This can potentially happen when firstly formed FeO or Fe_3O_4 , losing its oxygen to Cr and Si as the oxygen moving in. The oxygen coming in from the environment (LBE) is less than the rate of oxygen losing to Cr and Si. This can be further proved by Fig. 2(b), the most exterior of the Fe layer still shows O enrichment, so a very thin layer of FeO or Fe_3O_4 may still exist there.

4.3 Mechanisms and evolution of the corrosion process

Different kinds of intergranular internal corrosion can happen because of the continuous protective oxide layer. For the area without protective oxide layer, the oxygen will use martensite GBs as fast diffusion path and form the GB oxidation as shown in Fig. 1(a). For the area with protective oxide layer, the oxygen will diffuse into the material much slower. The formation of oxide layer on the material surface will consume large amount of Cr which will trigger the recrystallization of martensite to ferrite. The grain will change from lath structure to more equal-axis grains [13]. After the oxygen penetrates through the oxide layer, it will use the newly formed GBs of the ferrite as fast diffusion path and form the GB oxidation as shown in Fig. 1(b).

The corrosion morphology shown in Fig. 1(a)-(f) indicates a progression from predominantly intergranular internal oxidation to wide area corrosion. As shown in Fig. 9 and Fig. 10, the degradation evolves from the formation of coarse internal oxides to pronounced liquid-metal (LME) penetration within the grains. The mechanism has been discussed in the literatures. Chen proposed that the outwards diffusion of Fe gives rise to large amounts of vacancies in the steel matrix which further accumulate to cavities [27]. Because the cavities provide a more oxidizing local environment, the Cr will be oxidized and cause the Cr from surrounding area to diffuse to the oxides. Because of the lower Cr content of Cr depleted region and lower oxygen potential, the Cr depleted region keeps unoxidized at first. After the Cr from matrix diffuses to the depleted region and the accumulation of oxygen, it becomes possible to oxidize these areas. As a result, wide area oxidation as shown in Fig. 9 will form.

As the internal oxides thicken, the mismatch in mechanical properties between the oxide layer and the steel substrate generates local stresses [44]. These stresses promote cracking and eventual spallation of the oxide layer, as evidenced in Fig. 8 and *Supplementary Materials S5*. Once the oxide fractures or detaches, fresh steel is exposed to LBE, allowing further penetration along GBs and eventually into grain interiors. The repeated cycle of internal oxidation, dissolution by LBE, and oxide cracking produces the characteristic subsurface morphology observed in Fig. 10.

Through this iterative process, LBE progressively consumes alloying elements and disrupts the microstructure, reducing the load-bearing capacity and long-term integrity of T91. The observed transition from intergranular corrosion to wider area corrosion thus reflects the combined effects of rapid oxygen ingress, internal oxidation, liquid metal dissolution, and mechanically induced oxide degradation.

4.4 Phase transformation

Phase transformations are observed in both Fig. 6 and Fig. 11(d-e), and in each case, they coincide with pronounced local Cr depletion, as shown in Fig. 5(b) and Fig. 11(b). This relationship is further supported by comparing Fig. 11 and Fig. 12. Both areas are from the 506 h corroded sample and have no obvious corrosion observed because of the continuous Cr/Si oxide formed on the surface. Even so, subtle phase changes are visible in Fig. 12(d–e). A direct comparison of Fig. 11(b) and Fig. 12(b) shows that the former contains a substantially larger Cr-depleted region, aligning with the more extensive microstructural transformation observed.

Previous studies [13] have demonstrated that Cr depletion reduces the recrystallization temperature of the near-surface region in T91 F/M steel. At the

corrosion temperature used in this work (700 °C), the Cr-depleted martensitic laths therefore undergo recovery and recrystallization to form equiaxed ferrite grains, which subsequently coarsen through grain growth. During recovery, residual dislocation structures are annihilated, internal stresses decrease, and lattice misorientation is significantly reduced. The carbon released from the dissolution of Cr-rich carbides (as shown in Fig. 5(b) and Fig. 11(b)) does not hinder this ferritization process because its concentration remains below the solubility limit of C in ferrite at 700 °C.

4.5 Unaffected regions formation

The unaffected regions consistently exhibit a continuous and adherent oxide layer on the surface. The presence of a dense, protective oxide scale—typically Cr-rich—is known to suppress both oxygen ingress and liquid-metal dissolution, thereby preventing microstructural degradation beneath the surface [37, 38]. In addition, the wettability of LBE to oxides is far lower than that to bare metals, stopping the initiation of any dissolutive liquid metal corrosion mechanisms in these fully passivated regions. Maintaining such a continuous oxide layer is therefore critical for ensuring long-term corrosion resistance of T91 in LBE environments. Achieving this requires sufficient Cr availability at the surface to sustain Cr-enriched oxide formation, controlled oxygen potential in the LBE to avoid under- or over-oxidation, and microstructural conditions that minimize oxide cracking or spallation [45, 46]. Recent studies further emphasize that alloy design (eg: optimized Cr content, Si and Al added), surface treatments, and precise oxygen control are essential strategies for stabilizing protective oxide scales under high-temperature LBE exposure [47, 48]. Thus, the ability to retain a continuous,

mechanically stable oxide layer emerges as a central criterion for future improvements in corrosion resistance.

5. Conclusion

Based on the mechanistic analysis presented in discussion, the oxidation and corrosion behaviour of T91 exposed to oxygen-controlled LBE at 700 °C can be described by the following conclusions:

Corrosion follows GBs:

The corrosion process begins with intergranular internal corrosion with the Cr-enriched and Si-enriched oxides forming. In the reducing environment, the dissolution of elements (Cr, Ni, Fe...) plays the main role of the corrosion, which induce a corrosion pattern which does not following the GBs. In oxidising environment, the oxygen plays an important role. The corrosion process begins with the oxidation, and this process is controlled by both elements of T91 (Cr) and oxygen diffusion.

Fe displacement and Fe-enrich layer formation:

There is a layer of Fe enriched layer with BCC lattice structure observed at the outside surface. The EDX and EBSD results suggest this layer can be a ferritic steel which consist mainly of Fe. The Fe probably diffuses outwards from the inner oxide layer and forms Fe oxide, which later lose the oxygen to internal Cr/Si oxide.

Corrosion transitions from intergranular internal attack to wider area corrosion

The Fe outwards diffusion may leave plenty of vacancies which may accumulate into nano cavities. These cavities at the surface will act as fast paths for the oxygen which allows them to further oxidise the internal areas. With the Cr diffusion from matrix

and oxygen potential increasing, the localized oxidation will develop to wider area corrosion. Thicken and generate mechanical stresses due to mismatch with the steel substrate, ultimately causing oxide cracking and spallation. Once the oxide layer fractures, LBE penetrates into grain interiors, dissolving Fe, Cr, Si in rough proportion to their solubilities in LBE and accelerating subsurface degradation. The interplay of internal oxidation, dissolution, and repeated oxide fracture results in progressively wider area corrosion.

Cr depletion induces microstructural transformation from martensite to ferrite.

Regions with severe Cr depletion experience significantly reduced recrystallisation temperatures. At 700 °C, the Cr-depleted martensite undergoes recovery, decomposition, and recrystallisation into equiaxed ferrite grains, accompanied by reduced lattice misorientation and defect density. Carbon released from the dissolution of Cr-rich carbides remains below its solubility limit in ferrite and does not inhibit ferritization.

Continuous protective oxide layers are essential for corrosion resistance.

Unaffected regions consistently possess stable, adherent Cr-rich oxide scales that suppress both oxygen ingress and LBE dissolution. Maintaining such protective scales requires adequate Cr availability, controlled oxygen potential in LBE, and microstructures that resist oxide cracking or spallation. These findings highlight oxide-scale stability as a critical design parameter for improving long-term T91 performance in LBE systems.

Statement on the Use of Generative AI

During the preparation of this work, the authors used ChatGPT for English language correction and improvement of expression. After using this tool, the authors carefully reviewed and edited the content as needed and take full responsibility for the accuracy, originality, and integrity of the publication.

CRedit Authorship Contribution Statement

Minyi Zhang: Writing – original draft, Methodology, Investigation, Formal analysis, Conceptualization.

Zhou Weiyue: Writing – review & editing, Methodology.

Michael P. Short: Writing – review & editing, Supervision, Methodology, Conceptualization.

Paul A.J. Bagot: Supervision.

Michael P. Moody: Supervision, Methodology, Conceptualization.

Felix Hofmann: Writing – review & editing, Supervision, Methodology, Conceptualization.

Declaration of competing interest

The authors declare that they have no known competing financial interests or personal relationships that could have appeared to influence the work reported in this paper.

Acknowledgements

[EP/T002808/1](#), Simultaneous Corrosion/Irradiation Testing in Lead and Lead-Bismuth Eutectic: The Radiation Decelerated Corrosion Hypothesis (RC-3).

[EP/T011505/1](#), An Atomic-Scale Characterisation Facility for Active Nuclear Materials.

[NEUP 19-16754](#), Simultaneous Corrosion/Irradiation Testing in Lead and Lead-Bismuth Eutectic: The Radiation Decelerated Corrosion Hypothesis.

[EP/R010145/1](#), The authors acknowledge use of characterisation facilities within the David Cockayne Centre for Electron Microscopy, Department of Materials, University of Oxford, alongside financial support provided by the Henry Royce Institute.

Data availability

Will be added here.

Reference:

1. Gong, X., et al., *Atomic-scale dissolution corrosion mechanism of additively-manufactured 316L steels in liquid lead-bismuth eutectic*. *Acta Materialia*, 2025. **290**: p. 120963.
2. Zhang, M., et al., *Nano-scale corrosion mechanism of T91 steel in static lead-bismuth eutectic: A combined APT, EBSD, and STEM investigation*. *Acta Materialia*, 2024: p. 119883.
3. Davis, T.P., *Dispelling misconceptions of nuclear energy technology: How Generation IV nuclear reactors could become the key to achieving the Paris Agreement and the United Kingdom's net zero CO2 emissions target by 2050*. *Saint Anne's Academic Review*, 2019. **9**.
4. Garner, F.A., M.B. Toloczko, and B.H. Sencer, *Comparison of swelling and irradiation creep behavior of fcc-austenitic and bcc-ferritic/martensitic alloys at high neutron exposure*. *Journal of Nuclear Materials*, 2000. **276**(1-3): p. 123-142.
5. Davis, T.P., et al., *Atom probe characterisation of segregation driven Cu and Mn-Ni-Si co-precipitation in neutron irradiated T91 tempered-martensitic steel*. *Materialia*, 2020. **14**.
6. Kohyama, A., et al., *Low-activation ferritic and martensitic steels for fusion application*. *Journal of Nuclear Materials*, 1996. **233**: p. 138-147.
7. Kurata, Y. and S. Saito, *Temperature Dependence of Corrosion of Ferritic/Martensitic and Austenitic Steels in Liquid Lead-Bismuth Eutectic*. *Materials Transactions*, 2009. **50**(10): p. 2410-2417.
8. Alemberti, A., et al., *Overview of lead-cooled fast reactor activities*. *Progress in Nuclear Energy*, 2014. **77**: p. 300-307.
9. Rebak, R.B. and D.D. Ellis. *Passivation Characteristics of Ferritic Stainless Materials in Simulated Reactor Environments*. in *NACE CORROSION*. 2016. NACE.
10. Li, N., *Active control of oxygen in molten lead-bismuth eutectic systems to prevent steel corrosion and coolant contamination*. *Journal of Nuclear materials*, 2002. **300**(1): p. 73-81.
11. Popovic, M.P., et al., *Oxidative passivation of Fe-Cr-Al steels in lead-bismuth eutectic under oxygen-controlled static conditions at 700° and 800° C*. *Journal of Nuclear Materials*, 2019. **523**: p. 172-181.

12. Weisenburger, A., et al. *Stability of oxide layer formed on high-chromium steels in LBE under oxygen content and temperature fluctuation*. in *The 13th international conference on nuclear engineering abstracts*. 2005.
13. Zhang, M., et al., *Correlated chromium carbide dissociation and phase transformation in liquid lead-bismuth eutectic corroded T91 steel*. *Corrosion Science*, 2025. **249**: p. 112851.
14. Courouau, J.-L., et al., *Impurities and oxygen control in lead alloys*. *Journal of Nuclear Materials*, 2002. **301**(1): p. 53-59.
15. Barbier, F., et al., *Compatibility tests of steels in flowing liquid lead–bismuth*. *Journal of Nuclear Materials*, 2001. **295**(2-3): p. 149-156.
16. Tas, H., et al., *Liquid breeder materials*. *Journal of Nuclear Materials*, 1988. **155**: p. 178-187.
17. Simon, N., A. Terlain, and T. Flament, *The compatibility of austenitic materials with liquid Pb–17Li*. *Corrosion science*, 2001. **43**(6): p. 1041-1052.
18. Laverde, D., T. Gomez-Acebo, and F. Castro, *Continuous and cyclic oxidation of T91 ferritic steel under steam*. *Corrosion science*, 2004. **46**(3): p. 613-631.
19. Was, G., et al., *Corrosion and stress corrosion cracking in supercritical water*. *Journal of Nuclear Materials*, 2007. **371**(1-3): p. 176-201.
20. Guntz, G., et al., *The T91 book*. Vallourec Industries, 1990.
21. Short, M., R. Ballinger, and H. Hänninen, *Corrosion resistance of alloys F91 and Fe–12Cr–2Si in lead–bismuth eutectic up to 715 C*. *Journal of nuclear materials*, 2013. **434**(1-3): p. 259-281.
22. Short, M.P., *The Design of a functionally graded composite for service in high temperature lead and lead-bismuth cooled nuclear reactors*. 2010, Massachusetts Institute of Technology.
23. Meisnar, M., et al., *Low-energy EDX–A novel approach to study stress corrosion cracking in SUS304 stainless steel via scanning electron microscopy*. *Micron*, 2014. **66**: p. 16-22.
24. Shreir, L.L., *Corrosion: metal/environment reactions*. 2013: Newnes.
25. Berger, M.J., Coursey, J.S., Zucker, M.A., and Chang, J. *ESTAR, PSTAR, and ASTAR: Computer Programs for Calculating Stopping-Power and Range Tables for Electrons, Protons, and Helium Ions*. NIST Standard Reference Database 124 2017 2.2.2026]; Available from: https://physics.nist.gov/PhysRefData/Star/Text/ESTAR.html?utm_source=chatgpt.com.
26. Shen, Z., et al., *New insights into the oxidation mechanisms of a Ferritic-Martensitic steel in high-temperature steam*. *Acta Materialia*, 2020. **194**: p. 522-539.
27. Chen, K., L. Zhang, and Z. Shen, *Understanding the surface oxide evolution of T91 ferritic-martensitic steel in supercritical water through advanced characterization*. *Acta Materialia*, 2020. **194**: p. 156-167.
28. Shen, Z., et al., *New insights into the oxidation mechanisms of a Ferritic-Martensitic steel in high-temperature steam*. *Acta Materialia*, 2020. **194**: p. 522-539.
29. Chen, G., et al., *Ultrastable lubricating properties of robust self-repairing tribofilms enabled by in situ-assembled polydopamine nanoparticles*. *Langmuir*, 2020. **36**(4): p. 852-861.
30. Cairang, W., et al., *Simultaneous proton irradiation and dissolution corrosion of SS316L in liquid Pb-4Bi alloy*. *Corrosion Science*, 2025: p. 113010.

31. Zhou, Q., Z. Zheng, and Y. Gao, *Abnormal selective dissolution by the partial recrystallization in a plastically deformed austenitic stainless steel*. Corrosion Science, 2021. **188**: p. 109548.
32. de Souza Silva, E.M.F., G.S. da Fonseca, and E.A. Ferreira, *Microstructural and selective dissolution analysis of 316L austenitic stainless steel*. Journal of Materials Research and Technology, 2021. **15**: p. 4317-4329.
33. Martinelli, L., et al., *Comparative oxidation behaviour of Fe-9Cr steel in CO₂ and H₂O at 550 C: Detailed analysis of the inner oxide layer*. Corrosion Science, 2015. **100**: p. 253-266.
34. Martinelli, L., et al., *Oxidation mechanism of a Fe-9Cr-1Mo steel by liquid Pb-Bi eutectic alloy (Part I)*. Corrosion Science, 2008. **50**(9): p. 2523-2536.
35. Martinelli, L., et al., *Oxidation mechanism of an Fe-9Cr-1Mo steel by liquid Pb-Bi eutectic alloy at 470 C (Part II)*. Corrosion Science, 2008. **50**(9): p. 2537-2548.
36. Ellingham, H.J., *Reducibility of oxides and sulphides in metallurgical processes*. J. Soc. Chem. Ind, 1944. **63**(5): p. 125-160.
37. Young, D.J., *High temperature oxidation and corrosion of metals*. Vol. 1. 2008: Elsevier.
38. Birks, N., G.H. Meier, and F.S. Pettit, *Introduction to the high temperature oxidation of metals*. 2006: Cambridge university press.
39. Tan, L., X. Ren, and T.R. Allen, *Corrosion behavior of 9-12% Cr ferritic-martensitic steels in supercritical water*. Corrosion science, 2010. **52**(4): p. 1520-1528.
40. Bischoff, J. and A.T. Motta, *Oxidation behavior of ferritic-martensitic and ODS steels in supercritical water*. Journal of Nuclear Materials, 2012. **424**(1-3): p. 261-276.
41. Ye, Z., et al., *Oxidation mechanism of T91 steel in liquid lead-bismuth eutectic: with consideration of internal oxidation*. Scientific reports, 2016. **6**(1): p. 35268.
42. Tan, L., Y. Yang, and T. Allen, *Oxidation behavior of iron-based alloy HCM12A exposed in supercritical water*. Corrosion Science, 2006. **48**(10): p. 3123-3138.
43. Chen, Y., K. Sridharan, and T. Allen, *Corrosion behavior of ferritic-martensitic steel T91 in supercritical water*. Corrosion Science, 2006. **48**(9): p. 2843-2854.
44. Krishnamurthy, R. and D. Srolovitz, *Stress distributions in growing oxide films*. Acta materialia, 2003. **51**(8): p. 2171-2190.
45. Galerie, A., et al., *Stress and adhesion of chromia-rich scales on ferritic stainless steels in relation with spallation*. Materials Research, 2004. **7**: p. 81-88.
46. Bamba, G., et al., *Thermal oxidation kinetics and oxide scale adhesion of Fe-15Cr alloys as a function of their silicon content*. Acta Materialia, 2006. **54**(15): p. 3917-3922.
47. Vogt, J.-B. and I. Proriol Serre, *A review of the surface modifications for corrosion mitigation of steels in lead and LBE*. Coatings, 2021. **11**(1): p. 53.
48. Wang, H., et al., *Corrosion behavior and surface treatment of cladding materials used in high-temperature lead-bismuth eutectic alloy: A review*. Coatings, 2021. **11**(3): p. 364.